DOI: 10.24352/UB.OVGU-2018-667 TECHNISCHE MECHANIK, 38, 3, (2018), 286– 299
submitted: November 17, 2018

Phase-Field Modelling of Crack Propagation in Anisotropic Polycrystalline Materials

Z. Liu, D. Juhre

Polycrystalline materials are widely used in engineering and material science applications, e.g. automobile, aerospace or renewable energy. The macroscopic defects are generally strongly influenced by the fracture behavior of the polycrystalline materials at meso- and microscopic level. In this paper, the proposed phase-field model for anisotropic fracture, which accounts for the preferential cleavage directions within each randomly oriented crystal, as well as an anisotropic material behavior with cubic symmetries, has been used to simulate the complex crack pattern in solar-grade polycrystalline silicon. Furthermore, the proposed phase-field model allows to distinguish the loading under tension and compression. The finite element implementation of the model has been realized by using a monolithic solution scheme. Three representative numerical examples are carried out, i.e. anisotropic crack propagation (i) in a sole material, (ii) in a bi-material with different crack orientation and (iii) in multi-grains with randomly distributed anisotropy. It is demonstrated that the proposed phase-field model is capable of characterizing fracture propagation in anisotropic solids under static loading.

1 Introduction

Nowadays, many components and structures (machines and equipment) are designed by using various polycrystalline materials (Zhu et al., 2016), e.g. alloys, ceramics or metals, etc. Polycrystalline microstructure contains several varying size of grains, bonded together by grain boundaries (Saddow, 2012). At meso- and microscopic level, each grain has different material properties, e.g. crack orientation. Microscopic material properties of polycrystals can influence the damage behavior of materials at the macroscale level and hence it is necessary to analyze the fracture performances of polycrystals at the meso- and microscopic level. But in general, conventional methods of strength calculation cannot be used to simulate defects in polycrystals and simulation of inter- and transgranular crack propagation may be a major challenging task to study among many researchers (Sukumar et al., 2003; Richard and Sander, 2009; Infuso et al., 2014; Paggi and Reinoso, 2017).
The application ability of analytical methods for fracture problems are mostly limited so that only simple crack propagation problems can be solved. As crack propagation problems contain special characteristics, such as complex geometries, loading conditions and material behaviours, they must be simulated by using advanced numerical methods, such as the extended finite element method (XFEM), cohesive zone models (CZM) or VCCT-Linear elastic fracture mechanics (LEFM) (Msekh et al., 2015). However, the application of these methods in fracture mechanics has some limitations, like the modelling of crack-branching, among others.
Recently, the phase-field method has been widely used to simulate crack nucleation, curved crack propagation, crack branching and merging of cracks without serious difficulties (Ambati et al., 2015b). In this method, the sharp crack is replaced by the diffuse crack which is the so-called phase-field parameter that varies smoothly from 1 (intact material) to 0 (fully cracked material). Based on the variational formulation of Griffith's theory (Francfort and Marigo, 1998), a regularized presentation of the variational phase-field model of fracture was devised by Bourdin et al. (2000). The phase-field problem can be solved simultaneously or separately. The monolithic solution scheme has been developed by Kuhn and Müller (2010). They proposed a Ginzburg-Landau type evolution equation for crack propagation in linear elastic solids. Miehe et al. (2010) have used the staggered solution to solve damage evolution problems in an alternative manner. To avoid the crack propagation under compression loading, a tension-compression partition concept was firstly performed by Amor et al. (2009). In their model, the elastic strain energy has been split into volumetric and deviatoric contributions. Under compression, the degradation function is only coupled with the deviatoric part of the elastic strain energy. Numerous phase-field approaches of brittle fracture have been proposed in recent works by Borden et al. (2012), Weinberg and Hesch (2015), Wick (2017) or Teichtmeister et al. (2017), etc. Furthermore, the phase-field method has been extended to simulate brittle fracture in rubbery polymers (Miehe et al., 2015), ductile fracture (Miehe et al., 2016), composite failure (Liu and Juhre,

2017) and fatigue behavior (Alessi et al., 2018), among others.
Until now, the number of attempts of phase-field modelling of crack initiation and propagation in polycrystalline materials is very limited. Clayton and Knap (2015) carried out a phase-field model for 3D fracture propagation in polycrystalline materials at large strains. In this work, a second order tensor $\boldsymbol{\omega}$ was used to enforce the crack propagation along one preferential plane. Nguyen et al. (2017) have used as well this phase-field model for simulating the failure process in polycrystals whereas they extended the simulation by inserting cohesive zone elements in terms of grain boundaries to investigate the effect of interphase failure processes. Here, the elastic strain energy function was modified under compression and a staggered solution scheme within the finite element framework was used. Some selected parameters in the proposed anisotropic phase-field model were analyzed. Paggi et al. (2018) presented a phase field model for brittle fracture to apply it for crack propagation in solar-grade polycrystalline silicon. The isotropic phase-field model for brittle fracture (Ambati et al., 2015b) was applied whereas the value of the critical fracture toughness depends on the material orientation.
In this contribution, firstly, we introduce the phase-field model for isotropic and anisotropic brittle fracture, respectively. Next, the proposed phase-field model is used to simulate crack propagation. In particular, a monolithic solution scheme is formulated and a comprehensive parameter study for anisotropic fracture has been done. Representative numerical examples for crack propagation in solar-grade polycrystalline silicon are carried out. Specifically, the influences of the crack orientation of the crack path in polycrystalline materials are depicted.

2 Phase-field and Crack Surface Density Function

2.1 Isotropy of the Fracture Resistance

Consider an axial homogeneous bar with cross-section Γ of infinite length with a crack at the axial position $x = 0$ which is shown in Fig. 1(a). In the sharp crack topology, an order parameter $s(x) \in [0, 1]$ is described as (Miehe et al., 2010):

$$s(x) := \begin{cases} 0 & \text{for } x = 0 \\ 1 & \text{otherwise} \end{cases}, \tag{1}$$

where $s(x)$ takes the value 1 for intact material and 0 in case of a fully broken material (Fig. 1(b)). In the phase-field model, the sharp crack topology is replaced by the diffuse crack topology (Fig. 1(c)). This diffuse crack topology can be approximated by using a standard exponential function:

$$s(x) = 1 - e^{-|x|/2\kappa}, \tag{2}$$

in which κ is a diffuse parameter which defines the actual thickness of the crack. The Eq. (2) satisfies the ordinary differential equation

$$s - 4\kappa^2 s'' - 1 = 0\,, \tag{3}$$

with the boundary conditions: $s(0) = 0$ and $s(\pm\infty) = 1$ and where

$$I(s) = \frac{1}{2}\int_\Omega \left\{(1-s)^2 + 4\kappa^2 s'^2\right\} dx, \tag{4}$$

represents the quadratic functional of phase-field second order. Observing that $dV = \Gamma dx$ and the crack surface $I(1-e^{-|x|/2\kappa}) = 2\kappa\Gamma$, it can be shown that a second order Taylor expansion of the functional for the crack surface Γ_κ is defined as:

$$\Gamma_\kappa(s) := \frac{1}{2\kappa} I(s) = \frac{1}{4\kappa}\int_\Omega \left\{(1-s)^2 + 4\kappa^2 s'^2\right\} dx. \tag{5}$$

Using the solution of minimization of Eq. (5), the diffuse crack topology problem can be solved. In the multi-dimensional case, where an arbitrary bounded domain $\Omega \subset R^d (d \in [2, 3])$ and surface boundary conditions $\partial\Omega$ are considered, the crack $\Gamma_\kappa(s)$ can be denoted as:

$$\Gamma_\kappa(s) = \int_\Omega \gamma(s, \nabla s) dV, \tag{6}$$

with γ as the crack density function per unit volume:

$$\gamma(s, \nabla s) = \frac{(1-s)^2}{4\kappa} + \kappa |\nabla s|^2\,. \tag{7}$$

The Euler-Lagrange equation associated with the variational principle for fracture is considered as:

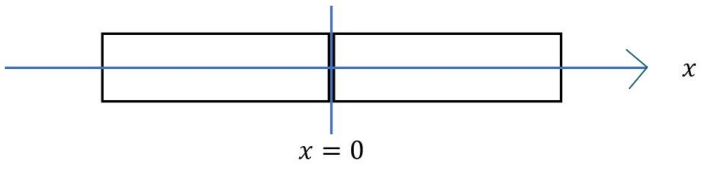

(a) cracked 1D Bar

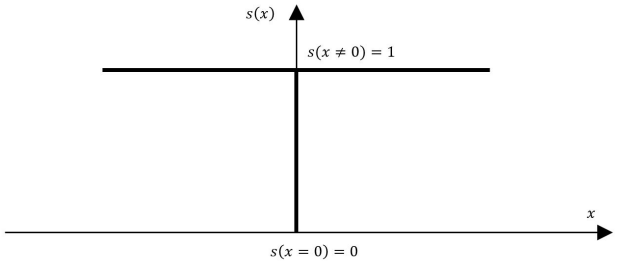

(b) sharp crack

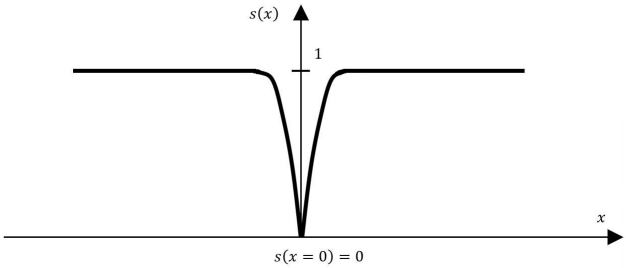

(c) diffuse crack

Figure 1: (a) 1D bar with a crack at $x = 0$. (b) Sharp crack topology at $x = 0$. (c) Diffuse crack topology at $x = 0$.

$$s - 4\kappa^2 \Delta s - 1 = 0 \ \text{ in } \ \Omega \ \text{ and } \nabla s \cdot \mathbf{n} = 0 \ \text{ on } \partial\Omega, \tag{8}$$

in which Δs is the Laplacian operation of the phase-field variable s and **n** is defined as the outward normal to $\partial\Omega$. A two-dimensional illustration of the phase-field method is depicted in Fig. 2.

2.2 Anisotropy of the Fracture Resistance

In the phase-field model for anisotropic brittle fracture, a second order structural tensor $\boldsymbol{\omega}$, being invariant with respect to rotations, as an additional material parameter for the directional dependency of the fracture resistance was introduced by Clayton and Knap (2015, 2016),

$$\boldsymbol{\omega} = \mathbf{1} + \beta \cdot (\mathbf{1} - \mathbf{M} \otimes \mathbf{M}), \tag{9}$$

where **1** denotes the second order identity tensor and $\otimes$ is the tensor product of two vectors. The vector **M** represents the unit vector normal to the preferential cleavage plane (with respect to the material coordinates). $\beta \gg 0$ denotes a penalty factor which mainly prevents the development of fracture on planes not normal to **M**. Note that in case of isotropic fracture resistance $\beta = 0$. In the two-dimensional case, the coefficients of the second order structural tensor $\boldsymbol{\omega}$ becomes

$$\boldsymbol{\omega} = \begin{pmatrix} 1 + \beta \sin^2(\theta) & -\beta \cos(\theta) \sin(\theta) \\ -\beta \cos(\theta) \sin(\theta) & 1 + \beta \cos^2(\theta) \end{pmatrix}, \tag{10}$$

and

$$\mathbf{M} = \begin{pmatrix} \cos(\theta) \\ \sin(\theta) \end{pmatrix}, \tag{11}$$

with the crack orientation θ. An illustration of the vector **M** and the crack orientation θ is shown in Fig. 3. Using this minor modification in the crack density functional, the fracture energy added by the phase-field gradient

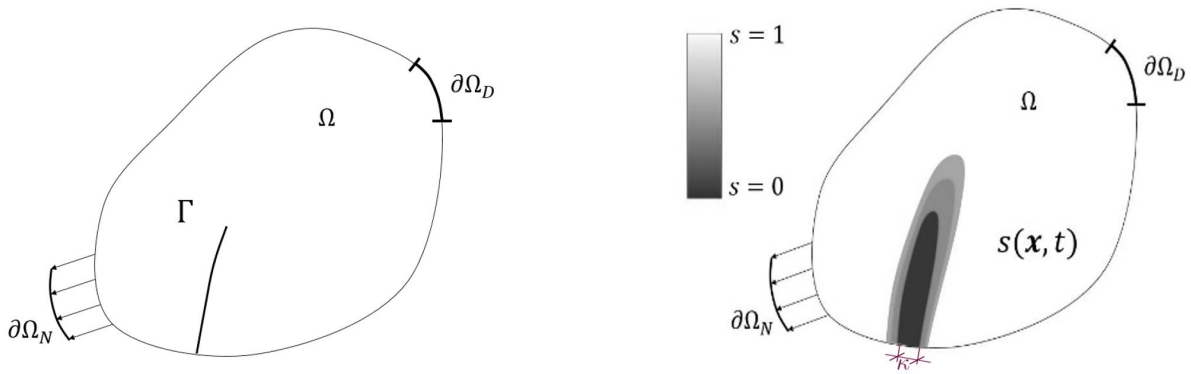

(a) sharp crack (b) diffuse crack

Figure 2: Illustration of the phase-field crack problem.

extension is oriented to the direction of the unit vector normal to the preferential cleavage plane. The crack density function γ per unit volume can be written as:

$$\gamma(s, \nabla s) = \frac{(1-s)^2}{4\kappa} + \kappa\, \boldsymbol{\omega} : (\nabla s \otimes \nabla s), \tag{12}$$

where the operator : is the double dot product of two tensors.

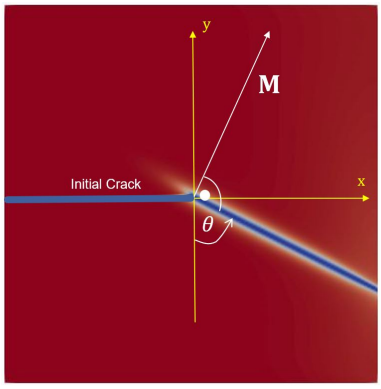

Figure 3: Illustration of the vector **M**, the unit vector normal to the preferential cleavage plane.

3 Phase-field Model

3.1 Phase-field Model of Anisotropic Fracture

In the variational theory of brittle fracture by Francfort and Marigo (1998), the variational principle for brittle fracture is the minimization of the total potential energy functional E and can be calculated as:

$$E(\boldsymbol{u}, \Gamma) = \int_\Omega \psi dV = \int_\Omega \underbrace{\frac{1}{2}\boldsymbol{\varepsilon} : (\mathbb{C} : \boldsymbol{\varepsilon})}_{\psi_e} dV + \int_\Gamma G_c d\Gamma, \tag{13}$$

with respect to the displacement field $\boldsymbol{u}$ which is discontinuous across the admissible crack set Γ. The entire (quasi-static) process of crack initiation and propagation can be determined by solving the minimization problem of the total potential energy functional E (Ambati et al., 2015a). Here, ψ_e is the elastic energy density of material with the linearized strain tensor $\boldsymbol{\varepsilon}$ and the fourth-order elastic stiffness tensor $\mathbb{C}$. In the following we want to focus only on cubic symmetry and hence, the principal stiffness matrix in 2D can be reduced to

$$\underline{\boldsymbol{C}} = \begin{pmatrix} C_{11} & C_{12} & 0 \\ C_{12} & C_{11} & 0 \\ 0 & 0 & C_{44} \end{pmatrix}, \tag{14}$$

whereas anisotropy is achieved if $C_{44} \neq (C_{11} - C_{12})/2$.
The Voigt notation of the anisotropic fourth-order elastic stiffness tensor can be expressed in matrix form as:

$$\boldsymbol{C} = \boldsymbol{P}\underline{\boldsymbol{C}}\boldsymbol{P}^T \quad \text{with} \quad \boldsymbol{C}(\alpha = 0^\circ) = \boldsymbol{C}(\alpha = 90^\circ), \tag{15}$$

where $\boldsymbol{P}$ is a matrix which transposes the principal stiffness matrix $\underline{\boldsymbol{C}}$ to the oriented stiffness matrix $\boldsymbol{C}$ in cartesian axes. The transformation matrix $\boldsymbol{P}$ can be formulated as (Li et al., 2015):

$$\boldsymbol{P} = \begin{pmatrix} \cos^2(\alpha) & \sin^2(\alpha) & 2\cos(\alpha)\sin(\alpha) \\ \sin^2(\alpha) & \cos^2(\alpha) & -2\cos(\alpha)\sin(\alpha) \\ -\cos(\alpha)\sin(\alpha) & \cos(\alpha)\sin(\alpha) & \cos^2(\alpha) - \sin^2(\alpha) \end{pmatrix}, \tag{16}$$

where α denotes the material orientation.
In Eq. (13), the critical energy release rate G_c denotes the critical energy required to create a unit area of new crack. To enable an efficient numerical treatment of Eq. (13), the elastic strain energy density is degraded with the function $g(s)$ which takes the form as:

$$\psi_e(\boldsymbol{\varepsilon}, s) = (g(s) + \eta)\frac{1}{2}\boldsymbol{\varepsilon} : (\boldsymbol{C} : \boldsymbol{\varepsilon}), \tag{17}$$

where the small positive dimensionless parameter $0 < \eta \ll 1$ is used to ensure a numerically well-conditioned system for a fully-broken state ($s = 0$). In Eq. (17), the degradation function $g(s)$ must be introduced to reduce the material stiffness after damage. In this paper, a quadratic function $g(s) = s^2$ is used and the phase-field s varies smoothly from 1 (intact material) to 0 (fully cracked material). The effects of using different quadratic, quartic and cubic degradation functions within the phase-field model have been investigated by Kuhn and Müller (2014). Using Eq. (12), the fracture energy can be approximated by

$$\int_\Gamma G_c d\Gamma = \int_V G_c \gamma(s, \nabla s) dV = \int_V \underbrace{G_c \left[\frac{(1-s)^2}{4\kappa} + \kappa \nabla s \cdot (\boldsymbol{\omega} \nabla s) \right]}_{\psi_f} dV, \tag{18}$$

in which ψ_f is the fracture energy density. If the diffuse parameter κ tends towards zero, the phase-field approximation of the fracture energy density ψ_f is exact (Kuhn and Müller, 2010). By substituting Eq. (17) and Eq. (18) into Eq. (13), the total energy density ψ can be defined as:

$$\psi(\boldsymbol{\varepsilon}, s) = (s^2 + \eta) \underbrace{\frac{1}{2}\boldsymbol{\varepsilon} : (\boldsymbol{C} : \boldsymbol{\varepsilon})}_{\psi_e} + \underbrace{G_c \left[\frac{(1-s)^2}{4\kappa} + \kappa \nabla s \cdot (\boldsymbol{\omega} \nabla s) \right]}_{\psi_f}, \tag{19}$$

The stress tensor $\boldsymbol{\sigma}$ is defined as the derivative of the total strain energy density with respect to the elastic strain tensor $\boldsymbol{\varepsilon}$:

$$\boldsymbol{\sigma} = \frac{\partial \psi}{\partial \boldsymbol{\varepsilon}} = (s^2 + \eta)\frac{\partial \psi_e}{\partial \boldsymbol{\varepsilon}} = (s^2 + \eta)\boldsymbol{C} : \boldsymbol{\varepsilon}. \tag{20}$$

Assuming neither dynamic contributions nor body loads, the local balance law can be obtained as:

$$\text{div}\, \boldsymbol{\sigma} = \boldsymbol{0}. \tag{21}$$

A time dependent Ginzburg-Landau evolution equation of the phase-field s which is variationally derived from the phase-field energy density is formulated as follows:

$$\frac{\dot{s}}{M} = -\frac{\delta \psi}{\delta s} = -\left[\frac{\partial \psi}{\partial s} - \text{div}\left(\frac{\partial \psi}{\partial \nabla s}\right) \right] = -2s\psi_e + G_c\left(\frac{1-s}{2\kappa} + 2\kappa \nabla s \cdot (\boldsymbol{\omega} \nabla s)\right), \tag{22}$$

where M is the mobility factor. In order to ensure crack propagation only under tensile or shear loading, a modified regularized formulation of the total strain energy density was proposed in (Amor et al., 2009), using the definition:

$$\psi(\boldsymbol{\varepsilon}, s) = (s^2 + \eta)\psi_e^+ + \psi_e^- + \psi_f, \tag{23}$$

with

$$\psi_e^+ = \frac{1}{2}\boldsymbol{\varepsilon}[\boldsymbol{C} - K\boldsymbol{1} \otimes \boldsymbol{1}\text{sign}^-(tr(\boldsymbol{\varepsilon}))]\boldsymbol{\varepsilon}, \tag{24}$$

$$\psi_e^- = \frac{1}{2} K \text{sign}^-(tr(\boldsymbol{\varepsilon}))\boldsymbol{\varepsilon}\mathbf{1} \otimes \mathbf{1}\boldsymbol{\varepsilon}, \tag{25}$$

whereas the corresponding bulk modulus is given as $K = (C_{11} + 2C_{12})/3$. The function $\text{sign}^-(tr(\boldsymbol{\varepsilon})) = 0$ if $tr(\boldsymbol{\varepsilon}) \geq 0$ and $\text{sign}^-(tr(\boldsymbol{\varepsilon})) = 1$ if $tr(\boldsymbol{\varepsilon}) < 0$. As a consequence the stress tensor $\boldsymbol{\sigma}$ takes the form

$$\boldsymbol{\sigma} = (s^2 + \eta) \underbrace{[\boldsymbol{C} - K\mathbf{1} \otimes \mathbf{1}\text{sign}^-(tr(\boldsymbol{\varepsilon}))]\boldsymbol{\varepsilon}}_{\boldsymbol{\sigma}^+ = \frac{\partial \psi_e^+}{\partial \boldsymbol{\varepsilon}}} + \underbrace{K\text{sign}^-(tr(\boldsymbol{\varepsilon}))\mathbf{1} \otimes \mathbf{1}\boldsymbol{\varepsilon}}_{\boldsymbol{\sigma}^- = \frac{\partial \psi_e^-}{\partial \boldsymbol{\varepsilon}}}. \tag{26}$$

Considering this modification the evolution equation can be rewritten as:

$$\frac{\dot{s}}{M} = -2s\,\psi_e^+ + G_c(\frac{1-s}{2\kappa} + 2\kappa\,\nabla s \cdot (\boldsymbol{\omega}\nabla s)). \tag{27}$$

In summary, the governing equations of the proposed phase-field model are reported in Table 1.

Table 1: Governing equations of the proposed phase-field model for brittle fracture

$\text{div}\,\boldsymbol{\sigma} = \mathbf{0}$
$\boldsymbol{\sigma} := (s^2 + \eta)\frac{\partial \psi_e^+}{\partial \boldsymbol{\varepsilon}} + \frac{\partial \psi_e^-}{\partial \boldsymbol{\varepsilon}}$
$\frac{\dot{s}}{M} = -2s\,\psi_e^+ + G_c(\frac{1-s}{2\kappa} + 2\kappa\nabla s \cdot (\boldsymbol{\omega}\nabla s))$

In the domain Ω, the partitions of the boundary satisfy the constraints:

$$\begin{cases} \boldsymbol{u} = \boldsymbol{u}^D & on\ \partial\Omega_D \\ \boldsymbol{\sigma} \cdot \mathbf{n} = \boldsymbol{t}^N & on\ \partial\Omega_N \\ \nabla s \cdot \mathbf{n} = 0 & on\ \partial\Omega_s \end{cases}, \tag{28}$$

where $\mathbf{n}$ is the outward pointing normal vector to the boundary, $\boldsymbol{t}^N$ as the prescribed traction force on Neumann boundary $\partial\Omega_N$ and $\boldsymbol{u}^D$ as prescribed displacement on Dirichlet boundary $\partial\Omega_D$, respectively.

4 Finite Element Formulation

The finite element implementation of the phase-field model for anisotropic fracture is explained in this section. The strong form of the balance equation Eq. (21) and the phase-field system Eq. (22) leads to the weak form with virtual displacement $\delta\mathbf{u}$ and virtual phase-field δs:

$$\int_{\partial\Omega_t} \delta\boldsymbol{u} \cdot \boldsymbol{t}^N\, dA - \int_\Omega (\nabla\delta\boldsymbol{u})^T : \boldsymbol{\sigma}\, dV = 0, \tag{29}$$

and

$$\int_\Omega [\delta s \frac{\dot{s}}{M} + 2\,G_c\kappa\,\nabla\,\delta s \cdot (\boldsymbol{w}\nabla s) + \delta s\,(2s\,\psi_e^+ - \frac{G_c}{2\kappa}(1-s))]dV = 0. \tag{30}$$

The discretization of the node values $\boldsymbol{u}_i$ and s_i in a 2D setting with Voigt notation can be expressed as:

$$\boldsymbol{u} = \sum_{i=1}^{n} N_i \boldsymbol{u}_i, \quad s = \sum_{i=1}^{n} N_i s_i, \tag{31}$$

where N_i is the shape function matrices for nodes i and n denotes the total number of nodes per element. $\boldsymbol{B}_i^u$ and $\boldsymbol{B}_i^s$ are matrices containing spatial derivatives of the shape functions of nodal displacement and nodal phase-field, respectively

$$\boldsymbol{B}_i^u = \begin{bmatrix} N_{i,x} & 0 & N_{i,y} \\ 0 & N_{i,y} & N_{i,x} \end{bmatrix}^T \text{and} \quad \boldsymbol{B}_i^s = \begin{bmatrix} N_{i,x} & N_{i,y} \end{bmatrix}^T, \tag{32}$$

and the gradient of the fields can be expressed as:

$$\boldsymbol{\varepsilon} = \sum_{i=1}^{n} \boldsymbol{B}_i^{\boldsymbol{u}} \boldsymbol{u}_i, \quad \nabla s = \sum_{i=1}^{n} B_i^s s_i. \tag{33}$$

The residual expression of element e at node i can be written as:

$$\boldsymbol{R}_i = \begin{bmatrix} \boldsymbol{R}_i^u \\ R_i^s \end{bmatrix} = \begin{bmatrix} \int_\Omega [\boldsymbol{B}_i^u]^T \, \boldsymbol{\sigma} \, dV \\ \int_\Omega N_i \frac{\dot{s}}{M} + [\boldsymbol{B}_i^s]^T (2G_c \, \kappa \, \boldsymbol{\omega} \, \nabla s) + N_i (2s \, \psi_e^+ + \frac{G_c}{2\epsilon}(s-1)) \, dV \end{bmatrix}. \tag{34}$$

The stiffness matrix $\boldsymbol{K}_{ij}$ for fully coupled simultaneous solution on the element level can be formulated as:

$$\boldsymbol{K}_{ij} = \begin{bmatrix} \boldsymbol{K}_{ij}^{uu} & \boldsymbol{K}_{ij}^{us} \\ \boldsymbol{K}_{ij}^{su} & K_{ij}^{ss} \end{bmatrix}, \tag{35}$$

where the stiffness submatrices are given as:

$$\begin{aligned} \boldsymbol{K}_{ij}^{uu} &= \int_\Omega [\boldsymbol{B}_i^u]^T \, \frac{\partial \boldsymbol{\sigma}}{\partial \boldsymbol{\epsilon}} \boldsymbol{B}_j^u \, dV, \\ \boldsymbol{K}_{ij}^{us} &= \int_\Omega [\boldsymbol{B}_i^u]^T \, \frac{\partial \boldsymbol{\sigma}}{\partial s} \, N_j \, dV, \\ \boldsymbol{K}_{ij}^{su} &= \int_\Omega N_i \, 2s \, \frac{\partial \psi_e^+}{\partial \boldsymbol{\varepsilon}} \, \boldsymbol{B}_j^u \, dV, \\ K_{ij}^{ss} &= \int_\Omega 2G_c \, \kappa \, [\boldsymbol{B}_i^s]^T \boldsymbol{\omega} \, \boldsymbol{B}_j^s + N_i (2\psi_e^+ + \frac{G_c}{2\kappa}) N_j \, dV, \end{aligned} \tag{36}$$

where $\frac{\partial \boldsymbol{\sigma}}{\partial \boldsymbol{\varepsilon}}$ takes the form as:

$$\frac{\partial \boldsymbol{\sigma}}{\partial \boldsymbol{\varepsilon}} = (s^2 + \eta)[\boldsymbol{C} - K\mathbf{1} \otimes \mathbf{1} \text{sign}^-(tr(\boldsymbol{\varepsilon}))] + K\mathbf{1} \otimes \mathbf{1} \text{sign}^-(tr(\boldsymbol{\varepsilon})). \tag{37}$$

$\frac{\partial \boldsymbol{\sigma}}{\partial s}$ and $\frac{\partial \psi_e^+}{\partial \boldsymbol{\varepsilon}}$ can be written as:

$$\frac{\partial \boldsymbol{\sigma}}{\partial s} = 2s \, \boldsymbol{\sigma}^+, \quad \frac{\partial \psi_e^+}{\partial \boldsymbol{\varepsilon}} = \boldsymbol{\sigma}^+. \tag{38}$$

Similar to the element stiffness matrix, the damping matrix is expressed as:

$$\boldsymbol{D}_{ij} = \begin{bmatrix} \boldsymbol{D}^{uu} & \boldsymbol{D}^{us} \\ \boldsymbol{D}^{su} & D^{ss} \end{bmatrix} = \begin{bmatrix} \mathbf{0} & \mathbf{0} \\ \mathbf{0} & \int_\Omega \frac{1}{M} N_i N_j \end{bmatrix} \, dV. \tag{39}$$

The submatrices of the element tangent matrix finally can be given as:

$$\boldsymbol{S}_{ij} = \boldsymbol{K}_{ij} + \frac{1}{\Delta t} \boldsymbol{D}_{ij}. \tag{40}$$

It is necessary to prevent unphysical crack healing (Schlüter et al., 2014), therefore, we define homogeneous Dirichlet boundary conditions, i.e. when $s \leq 0$ is reached for the time $t_{\mathbf{x}}^*$, $s(\mathbf{x}, t \geq t_{\mathbf{x}}^*) = 0$. This imposes a modification of the residual and the tangent matrix on element level in current time step t to realize

$$\Delta s_{i,m+1}^{(t)} = -s_{i,m+1}^{(t)} = 0. \tag{41}$$

In subsequent time step $t+1$, phase-field s remains as zero

$$s_{i,m+1}^{(t+1)} = s_{i,m+1}^{(t+1)} + \Delta s_{i,m+1}^{(t+1)} = s_{i,m+1}^{(t+1)} - s_{i,m+1}^{(t+1)} = 0. \tag{42}$$

The above algorithms have been implemented as a user defined element in FEAP (Taylor and Govindjee, 2017). The post-process for the plotting of results is supported by a visualization software Paraview (Ayachit, 2015). The multi-field coupled finite element problems are performed by using automatic step size control algorithms.

5 Numerical Examples

We demonstrate the potential of the proposed phase-field model to simulate the crack propagation in anisotropic materials by performing different numerical examples. At first we are focusing on crack propagation in a sole material and in a bi-material. These examples help to illustrate the effects of the anisotropic phase-field parameters

(penalty factor β and the crack orientation θ) on the fracture propagation. Finally, simulation of inter- and transgranular crack propagation are investigated and we highlight on the effects of anisotropy on the results.
The initial crack is modeled as a geometrical discontinuity by duplicated nodes (Miehe et al., 2010). The automatic loading step sizes for monolithic schemes is adopted. The phase-field model for anisotropic fracture has been implemented into a fully integrated 4-node quadrilateral plane strain element. The material properties in the numerical simulation are defined in Table 2 (Paggi et al., 2018). The principal stiffness matrix $\underline{\boldsymbol{C}}$ in a two dimension setting is chosen as follows:

$$\underline{\boldsymbol{C}} = \begin{pmatrix} 165700 & 63900 & 0 \\ 63900 & 165700 & 0 \\ 0 & 0 & 79600 \end{pmatrix} [N/mm^2], \tag{43}$$

with the corresponding bulk modulus $K = 97833.33\,[N/mm^2]$.

Table 2: Material parameters used in the numerical simulations.

Name	**Symbol**	**Value**	**Unit**
Stiffness resistance	η	10^{-6}	-
Critical energy release rate	G_c	2.04	N/mm
Mobility factor	M	1000	$mm^2/N \cdot s$

5.1 Crack Propagation in a Sole Material

Numerical simulations of anisotropic fracture for a square plane of unit length containing an initial crack located at mid-height of the left edge with a length of 0.5 mm are performed. The geometry and boundary conditions of the specimen are shown in Fig. 4. The complete top edge is moved by a vertical displacement. The spatial model is discretized by 40000 quadrilateral elements with an element size of $h = 0.005$ mm. The diffuse parameter κ is set to 0.005 mm. The displacement control with a minimum displacement increment (1.0E-7 mm) and a maximum displacement increment (5.0E-3 mm) is applied.

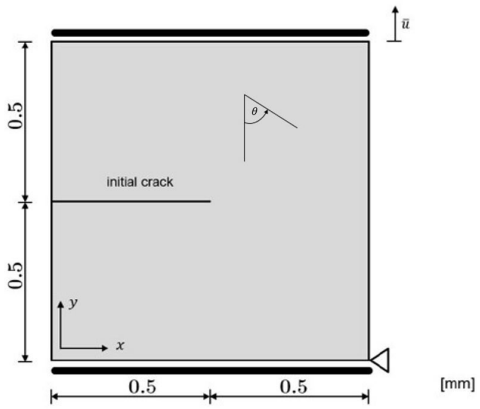

Figure 4: Geometry and boundary conditions

5.1.1 Variation of the Penalty Factor β

The crack propagation in anisotropic materials with cubic symmetries has been solved using the proposed phase-field model for varying the penalty factor β. The crack orientation θ and the material orientation α are fixed at $\theta = 45°$ and $\alpha = -45°$, respectively. The penalty factor β is varied in a range from 0 to 20. Fig. 5 presents the resulting crack paths for different penalty factors β. The crack propagates as expected in the horizontal direction in the case of isotropic fracture $\beta = 0$. It can be observed that the crack path changes when $\beta \neq 0$. For $0 < \beta < 1$, the crack orientation is hardly influenced. For $\beta > 1$, the crack orientation is obviously strongly influenced and it converges to the pre-defined angle of crack orientation θ by increasing β. The results show that the crack orientation in anisotropic materials significantly depends on the chosen value of the penalty factor β.

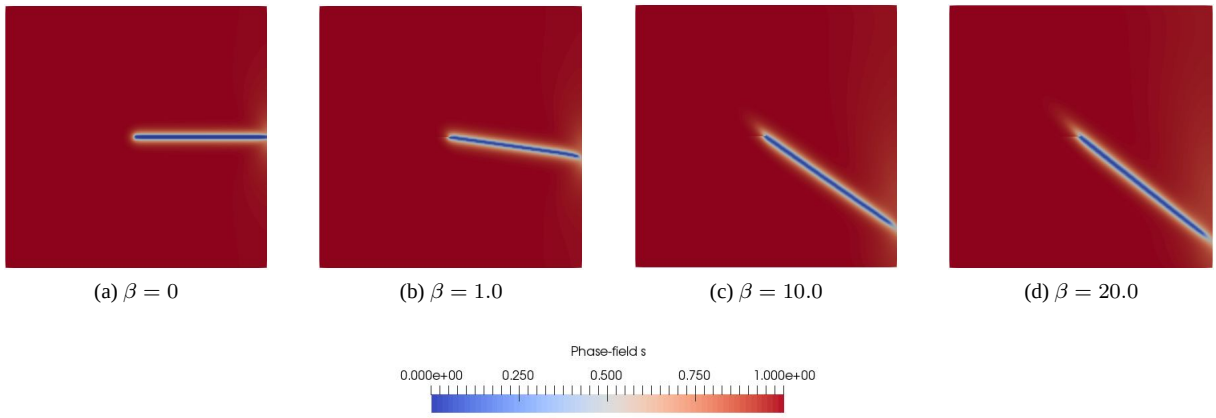

(a) $\beta = 0$ (b) $\beta = 1.0$ (c) $\beta = 10.0$ (d) $\beta = 20.0$

Figure 5: Influence of the penalty factor β on the direction of the crack path.

5.1.2 Variation of the Crack Orientation θ

In anisotropic materials with cubic symmetries, crack path is strongly influenced by the crack orientation θ, as depicted in (Clayton and Knap, 2015). For the simulations the penalty factor and material orientation are held constant at $\beta = 20$ and $\alpha = 0°$, respectively. The resulting crack paths obtained with the proposed model and with different directions of anisotropy θ are shown in Fig. 6. For $\theta = 90°$ (Fig. 6(a)) up to $\theta = 20°$ (Fig. 6(d)) the crack propagates as expected, following the predefined crack orientation. However, if we choose $\theta = 10°$ (Fig. 6(e)) or even lower, the resulting crack path is no longer in alignment with the predefined crack orientation. It rather follows the opposite direction with fluctuating crack paths (Fig. 6(e) - (g))) and finally results in a diffuse horizontally aligned crack for $\theta = 0°$ (Fig. 6(h)). Also Bleyer and Alessi (2018) have already shown this phenomena exclusively for the case of $\theta = 0°$. However, the reason for these findings are until now not clarified, neither analytically nor experimentally, and has to be investigated in future studies.

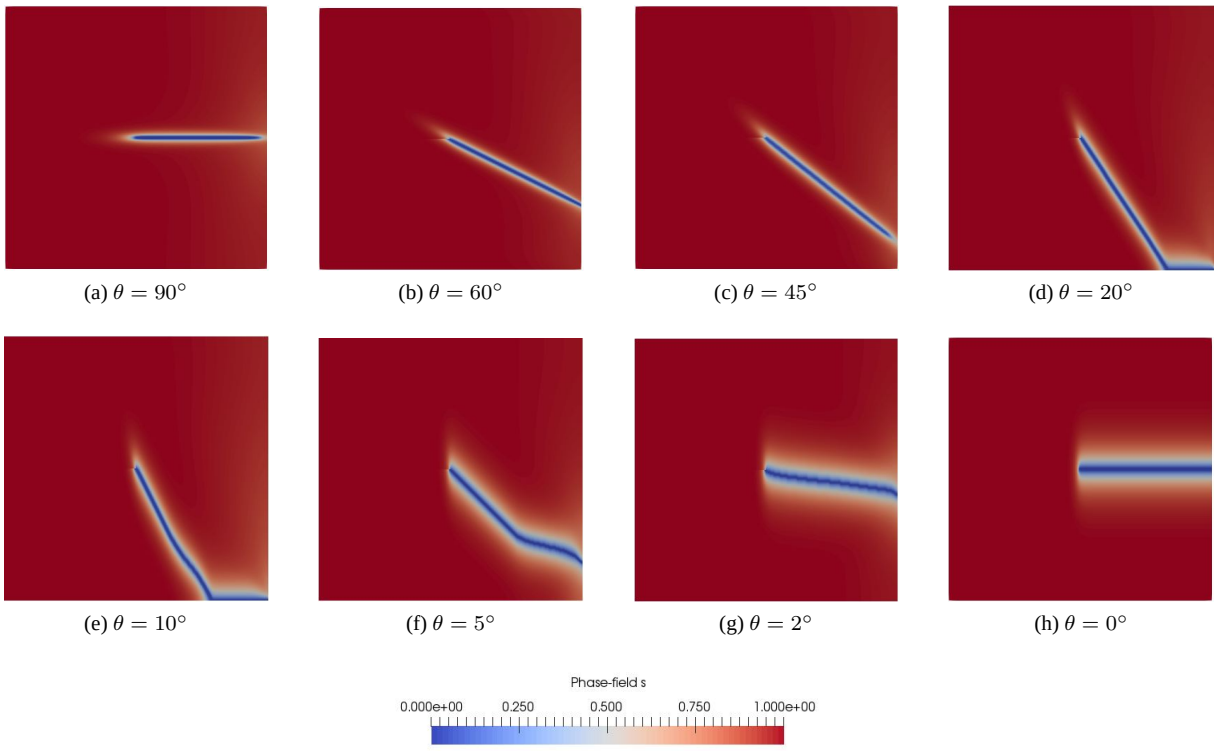

(a) $\theta = 90°$ (b) $\theta = 60°$ (c) $\theta = 45°$ (d) $\theta = 20°$

(e) $\theta = 10°$ (f) $\theta = 5°$ (g) $\theta = 2°$ (h) $\theta = 0°$

Figure 6: Influence of crack orientation θ on the crack path.

5.2 Crack Propagation in a Bi-material

As next, we examine the notched specimen consisting of bi-materials under tensile loading. The Fig. 7 shows the geometry and boundary conditions. The effective element size is chosen to be 0.05 mm using a fully integrated 4-node quadrilateral plane strain element. The material parameters are listed in Table 2 including $\kappa = 0.05$ mm, $\beta = 20$ and $\alpha = 0°$. We aim to analyze that how the crack propagates along material boundaries. The crack orientation in material 1 is set to $\theta_1 = 45°$ and the crack orientation in material 2 is varied in a range from $\theta_1 = 90°$ to $\theta_2 = -90°$. The results in Fig. 8 show that, except for $\theta_2 = -30°$ (Fig. 8(e)), all configurations lead to a transgranular fracture. After the crack crosses the material boundary, it propagates in the direction which correlates to θ. It can also be observed that each crack orientation only influences the crack direction in its own material domain. On the contrary, for the case $\theta_2 = -30°$, the crack orientation is greater than the angle between the material boundary and x-coordinates, resulting that the crack crosses nearly the material boundary. In other words, intergranular fracture depends on the orientation of material boundaries and the angle of crack orientation.

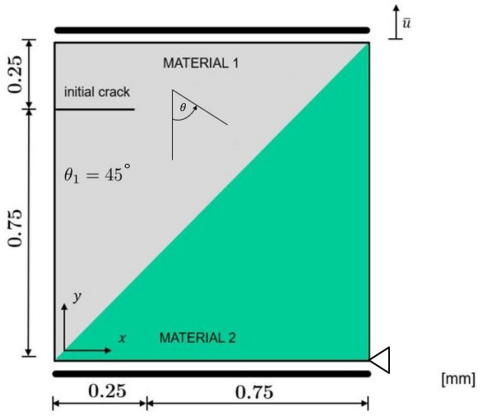

Figure 7: Geometry and boundary conditions

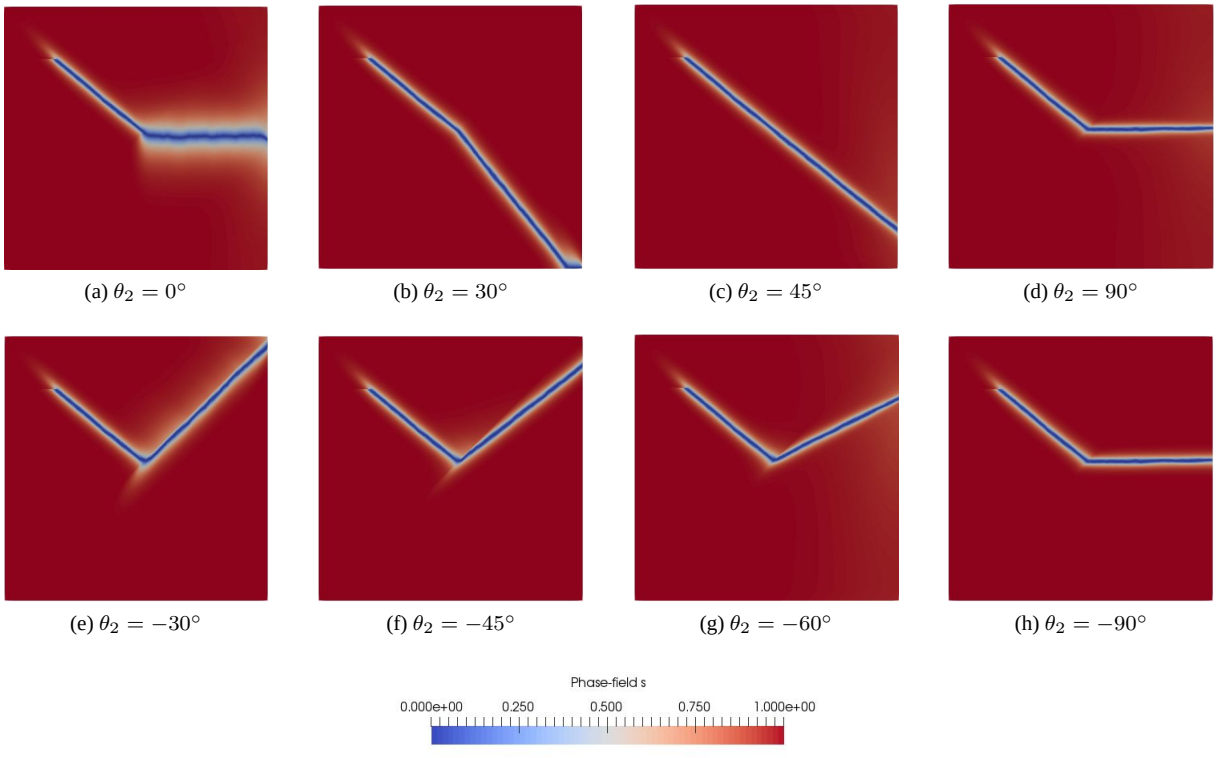

(a) $\theta_2 = 0°$ (b) $\theta_2 = 30°$ (c) $\theta_2 = 45°$ (d) $\theta_2 = 90°$

(e) $\theta_2 = -30°$ (f) $\theta_2 = -45°$ (g) $\theta_2 = -60°$ (h) $\theta_2 = -90°$

Figure 8: Influence of the crack orientation θ on the crack path.

5.3 Crack Propagation in Polycrytalline Materials

To demonstrate the numerical performance of the proposed phase-field model for anisotropic fracture in solar-grade polycrystalline silicon (Paggi et al., 2018), crack growth in a square polycrystalline microstructure with 10 mm $\times$ 10 mm domain consisting of an initial crack and 10 grains under uniaxial tension is simulated. The details of the geometry and boundary conditions are schematically shown in Fig. 9(a). Each grain has been associated a randomly crack orientation, as depicted in Fig. 9(b). The material parameters are listed in Table 2. The unstructured mesh consists of 50141 quadrilateral elements with a mean element size h of 0.05 mm. The diffuse length κ is considered as the same value as h.

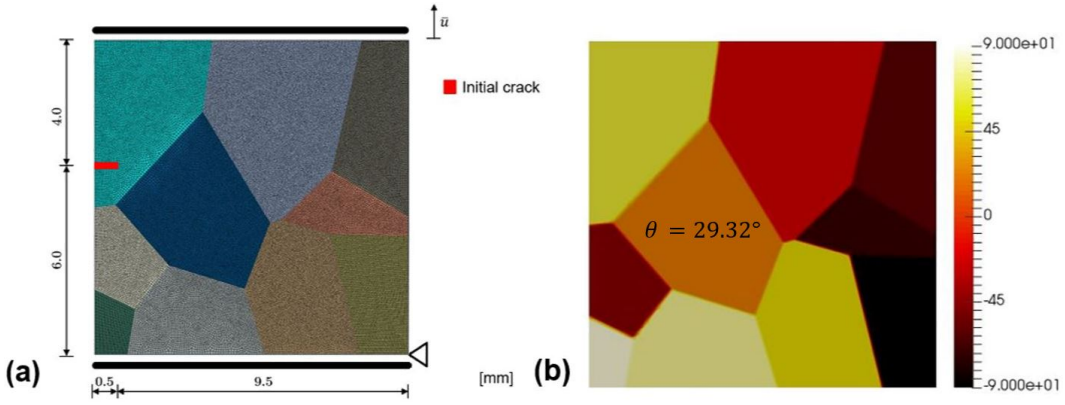

Figure 9: (a) Geometry and boundary conditions for the polycrystalline structure containing 10 grains; (b) Angle of the crack orientation.

Fig. 10(a) - (d) depict the evolution of the crack phase-field at several failure stages under tensile loading. In each transgranular fracture system, the direction of the crack path appears not identical. Fig. 10(c) shows that the crack runs within the grain boundary from the secondary transgranular fracture system and the crack swifts to the neighboring grain. A phenomenon for inter- and transgranular fracture can be observed for the numerical results that the crack orientation influences the crack propagation in each transgranular fracture system. The intergranular fracture will take place mainly when the orientation of the boundary of grains resists the crack propagation from transgranular fracture system.

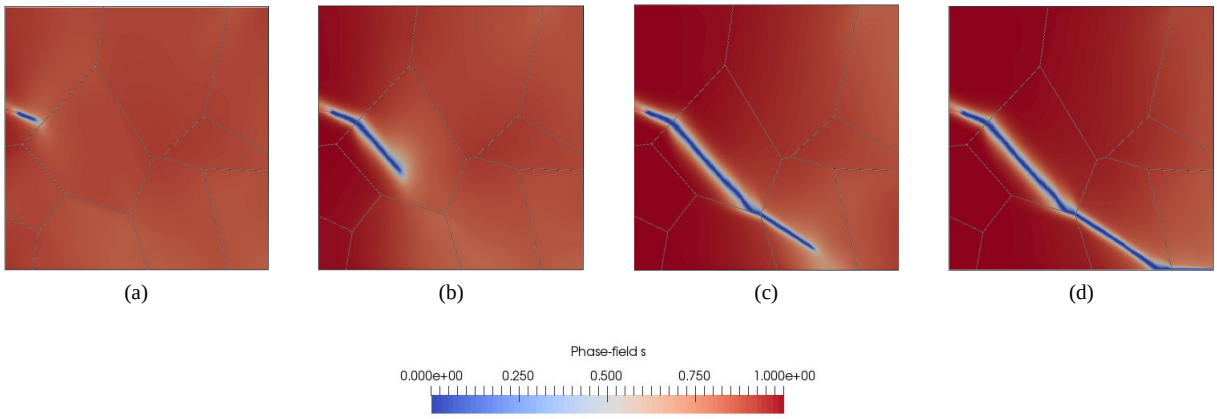

Figure 10: Crack phase-field at various fracture stages.

The same arrangement of polycrystals is used for another simulation in which the crack orientation in one grain is changed from 29.32° to 0° (see Fig. 11(a)). All the other settings remain as before. The impact of this modification is shown in Fig. 11(b). It can be observed that the crack propagates nearly horizontally in the modified grain

due to the change of the crack orientation. Obviously, the resulting crack path may be changed by defining a new crack orientation for another involved grain. It signifies that the anisotropic properties within each grain can strongly affect the microscopic crack propagation. Hence, for a detailed investigation of such cracks the anisotropic properties should be taken into account.

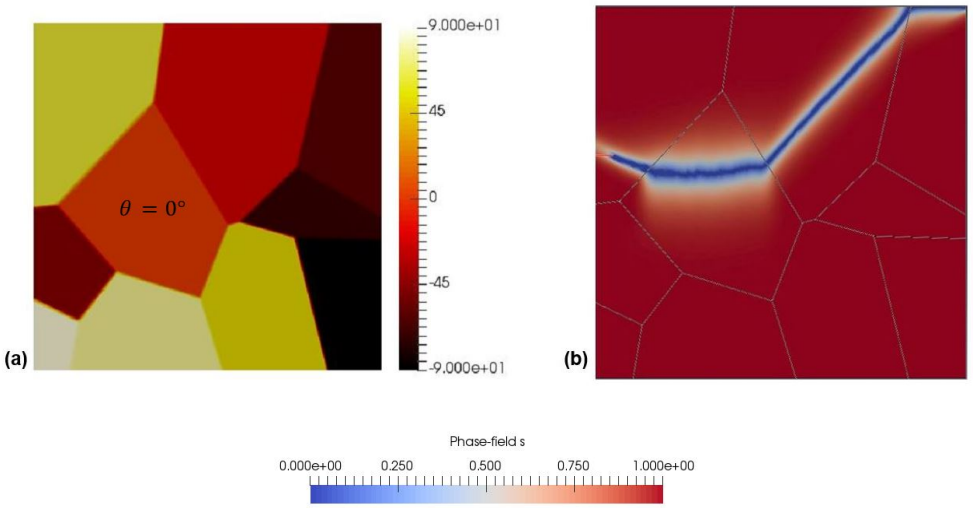

Figure 11: (a) Crack orientation; (b) Crack phase-field at final failure stage.

6 Conclusions

In this contribution, we firstly provided a brief overview of the phase-field model for crack propagation in isotropic and anisotropic materials, respectively. Next, we presented the phase-field model for anisotropic fracture which can distinguish the loading under tension and compression. The fully coupled monolithic solution scheme within the finite element framework was formulated. Comprehensive parameter studies for the proposed phase-field model have been done and the results have been analyzed. Simulations of the anisotropic fracture within the lower value of the crack orientation θ are also considered, though the resulting crack path is no longer in alignment with the predefined crack orientation, and the opposite direction with fluctuating crack paths can be observed in the results. Furthermore, it is necessary to account for such phenomena that the widely used anisotropic materials (e.g. woods) consist of the lower value of the crack orientation in the structure and it can play an important role in material design processes. This topics will be addressed elsewhere. Representative numerical examples of the crack propagation in solar-grade polycrystalline silicon are carried out which can validate its capability of modelling of inter- and transgranular fracture process. Last but not least, the damage and failure analysis of solar-grade polycrystalline silicon using phase-field method will also be compared with experimental results in future.

Acknowledgement

This work was supported by the program of the Federal State of Saxony-Anhalt, Germany. This support is grateful acknowledged.

References

Alessi, R.; Vidoli, S.; De Lorenzis, L.: A phenomenological approach to fatigue with a variational phase-field model: The one-dimensional case. *Eng. Fract. Mech.*, 190, (2018), 53 – 73.

Ambati, M.; Gerasimov, T.; De Lorenzis, L.: Phase-field modeling of ductile fracture. *Comput. Mech.*, 55, (2015a), 1017 – 1040.

Ambati, M.; Gerasimov, T.; De Lorenzis, L.: A review on phase-field models of brittle fracture and a new fast hybrid formulation. *Comput. Mech.*, 55, (2015b), 383 – 405.

Amor, H.; Marigo, J.; Maurini, C.: Regularized formulation of the variational brittle fracture with unilateral contact: Numerical experiments. *J. Mech. Phys. Solids.*, 57, (2009), 1209 – 1229.

Ayachit, U.: *The ParaView Guide: A Parallel Visualization Application*. Kitware, Inc., USA (2015).

Bleyer, J.; Alessi, R.: Phase-field modeling of anisotropic brittle fracture including several damage mechanisms. *Comput. Methods Appl. Mech. Eng.*, 336, (2018), 213 – 236.

Borden, M.; Verhoosel, C.; Scott, M.; Hughes, T.; Landis, C.: A phase-field description of dynamic brittle fracture. *Comput. Methods Appl. Mech. Eng.*, 217 – 220, (2012), 77 – 95.

Bourdin, B.; Francfort, G.; Marigo, J.: Numerical experiments in revisited brittle fracture. *J. Mech. Phys. Solids.*, 48 (4), (2000), 797 – 826.

Clayton, J.; Knap, J.: Phase field modeling of directional fracture in anisotropic polycrystals. *Comput. Mater. Sci.*, 98, (2015), 158 – 169.

Clayton, J.; Knap, J.: Phase field modeling and simulation of coupled fracture and twinning in single crystals and polycrystals. *Comput. Methods Appl. Mech. Eng.*, 312, (2016), 447 – 467.

Francfort, G.; Marigo, J.: Revisiting brittle fracture as an energy minimization problem. *J. Mech. Phys. Solids.*, 46 (8), (1998), 1319 – 1342.

Infuso, A.; Corrado, M.; Paggi, M.: Image analysis of polycrystalline solar cells and modelling of intergranular and transgranular cracking. *J. Eur. Ceram. Soc.*, 34 (11), (2014), 2713 – 2722.

Kuhn, C.; Müller, H.: A continuum phase field model for fracture. *Eng. Fract. Mech.*, 77, (2010), 3625 – 3643.

Kuhn, C.; Müller, H.: Simulation of size effects by a phase field model for fracture. *TAML.*, 5, (2014), 051008.

Li, B.; Peco, C.; Millán, D.; Arias, I.; Arroyo, M.: Phase-field modeling and simulation of fracture in brittle materials with strongly anisotropic surface energy. *Int. J. Numer. Meth. Eng.*, 102, (2015), 711 – 727.

Liu, Z.; Juhre, D.: Phase-field modelling of crack propagation in elasto-plastic multilayered materials. In: *Proceedings of the 7th GACM Colloquium on Computational Mechanics for Young Scientists from Academia and Industry* (2017).

Miehe, C.; Aldakheel, F.; Raina, A.: Phase field modeling of ductile fracture at finite strains: A variational gradient-extended plasticity-damage theory. *Int. J. Plast.*, 84, (2016), 1 – 32.

Miehe, C.; Hofacker, M.; Welschinger, F.: A phase field model for rate-independent crack propagation: robust algorithmic implementation based on operator splits. *Comput. Methods Appl. Mech. Eng.*, 199, (2010), 2765 – 2778.

Miehe, M.; Schänzel, L.; Ulmer, H.: Phase field modeling of fracture in multi-physics problems. part i. balance of crack surface and failure criteria for brittle crack propagation in thermo-elastic solids. *Comput. Methods Appl. Mech. Eng.*, 294, (2015), 449 – 485.

Msekh, M.; Sargado, J.; Jamshidian, M.; Areias, P.; Rabczuk, T.: Abaqus implementation of phase-field model for brittle fracture. *Comput. Mater. Sci.*, 96, (2015), 472 – 484.

Nguyen, T.; Réthoré, J.; Yvonnet, J.; Baietto, M.: Multi-phase-field modeling of anisotropic crack propagation for polycrystalline materials. *Comput. Mech.*, 60, (2017), 1 – 26.

Paggi, M.; Corrado, M.; Reinoso, J.: Fracture of solar-grade anisotropic polycrystalline silicon: A combined phase fieldcohesive zone model approach. *Comput. Methods Appl. Mech. Eng.*, 330, (2018), 123 – 148.

Paggi, M.; Reinoso, J.: Revisiting the problem of a crack impinging on an interface: A modeling framework for the interaction between the phase field approach for brittle fracture and the interface cohesive zone model. *Comput. Methods Appl. Mech. Eng.*, 321, (2017), 145 – 172.

Richard, H.; Sander, M.: *Ermüdungsrisse. Erkennen, sicher beurteilen, vermeiden*. Springer-Verlag, Berlin (2009).

Saddow, S. E.: *Silicon Carbide Biotechnology (Second Edition)*. Elsevier-Verlag, München (2012).

Schlüter, A.; Willenbücher, A.; Kuhn, C.; Müller, R.: Phase field approximation of dynamic brittle fracture. *Comput. Mech.*, 54, 5, (2014), 1141 – 1161.

Sukumar, N.; Srolovitz, D.; Baker, T.; Prévost, J.: Brittle fracture in polycrystalline microstructures with the extended finite element method. *Int. J. Numer Meth. Eng.*, 56 (14), (2003), 2015 – 2037.

Taylor, R. L.; Govindjee, S.: FEAP - finite element analysis program (2017).

Teichtmeister, S.; Kienle, D.; Aldakheel, F.; Keip, M. A.: Phase field modeling of fracture in anisotropic brittle solids. *Int. J. Nonlinear Mech.*, 97, (2017), 1 – 21.

Weinberg, K.; Hesch, C.: A high-order finite deformation phase-field approach to fracture. *Continuum. Mech. Therm.*, 19, (2015), 1 – 11.

Wick, T.: Modified newton methods for solving fully monolithic phase-field quasi-static brittle fracture propagation. *Comput. Methods Appl. Mech. Eng.*, 325, (2017), 577 – 611.

Zhu, N.; De Meo, D.; Oterkus, E.: Modelling of granular fracture in polycrystalline materials using ordinary state-based peridynamics. *Materials (Basel)*, 9, (2016), 977.

Address: Otto-von-Guericke-Universität Magdeburg, Institut für Mechanik, Universitätsplatz 2, D-39106 Magdeburg, Germany
email: zhengkun.liu@ovgu.de | daniel.juhre@ovgu.de